



## The rose petal effect and the role of advancing water contact angles for drop confinement

Mandsberg, Nikolaj Kofoed ; Taboryski, Rafael J.

*Published in:*  
Surface Topography: Metrology and Properties

*Link to article, DOI:*  
[10.1088/2051-672X/aa6855](https://doi.org/10.1088/2051-672X/aa6855)

*Publication date:*  
2017

*Document Version*  
Peer reviewed version

[Link back to DTU Orbit](#)

*Citation (APA):*  
Mandsberg, N. K., & Taboryski, R. J. (2017). The rose petal effect and the role of advancing water contact angles for drop confinement. *Surface Topography: Metrology and Properties*, 5, Article 024001. <https://doi.org/10.1088/2051-672X/aa6855>

---

### General rights

Copyright and moral rights for the publications made accessible in the public portal are retained by the authors and/or other copyright owners and it is a condition of accessing publications that users recognise and abide by the legal requirements associated with these rights.

- Users may download and print one copy of any publication from the public portal for the purpose of private study or research.
- You may not further distribute the material or use it for any profit-making activity or commercial gain
- You may freely distribute the URL identifying the publication in the public portal

If you believe that this document breaches copyright please contact us providing details, and we will remove access to the work immediately and investigate your claim.

## The rose petal effect and the role of advancing water contact angles for drop confinement

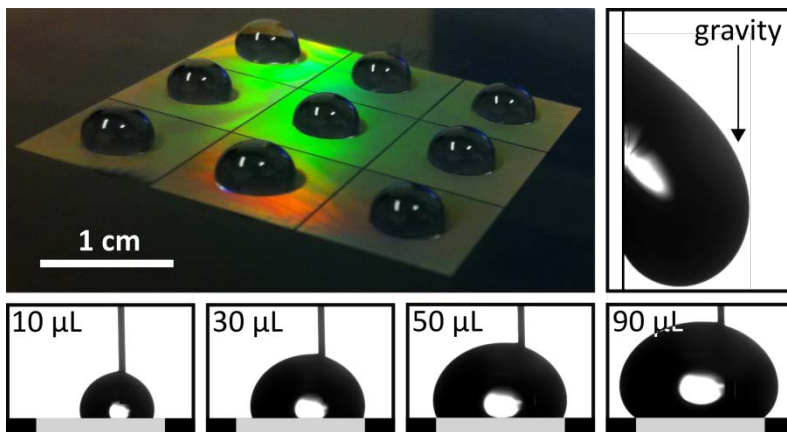
Nikolaj Kofoed Mandsberg and Rafael Taboryski\*

Department of Micro- and Nanotechnology, Technical University of Denmark, 2800 Kongens Lyngby, Denmark

\* [rata@nanotech.dtu.dk](mailto:rata@nanotech.dtu.dk)

**Key words:** Rose petal, advancing contact angle, triple phase boundary line, superhydrophobic, self-alignment, biomimetic surface, droplet pinning, surface wetting,

### Table of content graphic



### Abstract

We studied the role of advancing water contact angles on superhydrophobic surfaces that yet exhibited strong pinning effects as known in nature from rose petals. Textured surfaces were engineered in silicon by lithographical techniques. The textures were comprised of hexagonal microstructures superimposed with randomly distributed nanospikes and were coated with a hydrophobic fluorocarbon agent. A step in the advancing water contact angle bounding specific areas was obtained by engineering a corresponding topographic step in the hexagonal micro-texture. This enabled a surface texture design confining drops to areas with the lower advancing contact angle.

## Introduction

The interaction between liquids and surfaces is an important research topic that has been widely explored for decades due to the promising applications in a wide range of areas such as self-cleaning, anti-icing, drag reduction, anti-fogging, anti-fouling, and microfluidics. [1-9] Some of the earlier descriptions deal with the wetting state of liquids on heterosurfaces.[10, 11] A couple of decades ago the lotus-effect was discovered [12] and spawned a huge interest for the engineering of self-cleaning (superhydrophobic) surfaces.[13] However, while the repelling of liquids has been widely studied, we believe that the liquid surface adhesion, when further explored, has potential for even more applications, due to the variable degree of interaction. To this end, another biomimetic effect, the rose petal effect, sometimes also referred to as the Cassie-impregnating state,[14-17] with its extreme pinning effect, is particularly interesting. The rose petal effect has been widely studied,[18-20] and is also the subject of interest in this paper. A few other examples of recent studies that we here build upon are; the numerical studies of pinning and depinning on chemically patterned surfaces,[21] the pinning due to a topographic ring,[22] pinning when a wettability contrast is present,[23] and trapping of sliding drops by wetting defects[24].

From an engineering point of view, the up-scaling aspect is of major concern. Hence, the surfaces should preferably be compatible with techniques of mass replication, such as Si micro-fabrication, [17, 25, 26], nano-imprint lithography,[27] injection molding,[17, 28] or polymer replication by roll-to-roll processes [29, 30]. For this reason we shall deal with chemically homogeneous surfaces as the fabrication of these is compatible with the mentioned techniques; in addition, the replication process is simpler as it does not require a fabrication a step with chemical patterning[31].

In their article on chemical steps, Semprebon et al (2016) [32] showed how contact angle hysteresis can be exploited to direct and control liquid drops. Here we develop upon this idea and facilitate a step in the wetting properties, but through pure surface topography. By inflating drops across the step, we show how the advancing contact angle plays a crucial role for drops subject to the rose petal effect. Furthermore, we exploit this effect to create a surface with self-aligning properties, which additionally allows access to almost any desired contact angle using only two different microscopic wetting structures.

The investigated surface is shown in **Figure 1**. It consists of a hierarchical structure comprising a two-level hexagonal micro-pit structure superimposed with a random nanograss texture. The hexagonal micro-pit pattern has linewidth  $a$ , side length  $s$  and a step in depth between an inner shallow area with depth  $h$ , where drops are placed, and an outer area with larger depth  $H$ . Both areas have the same hydrophobic

surface chemistry. Drops pipetted to the inner shallow area and subsequently inflated tend to align to the center and remain in this area, until the whole area is filled, and the drop matches the advancing contact angle of the outer area.

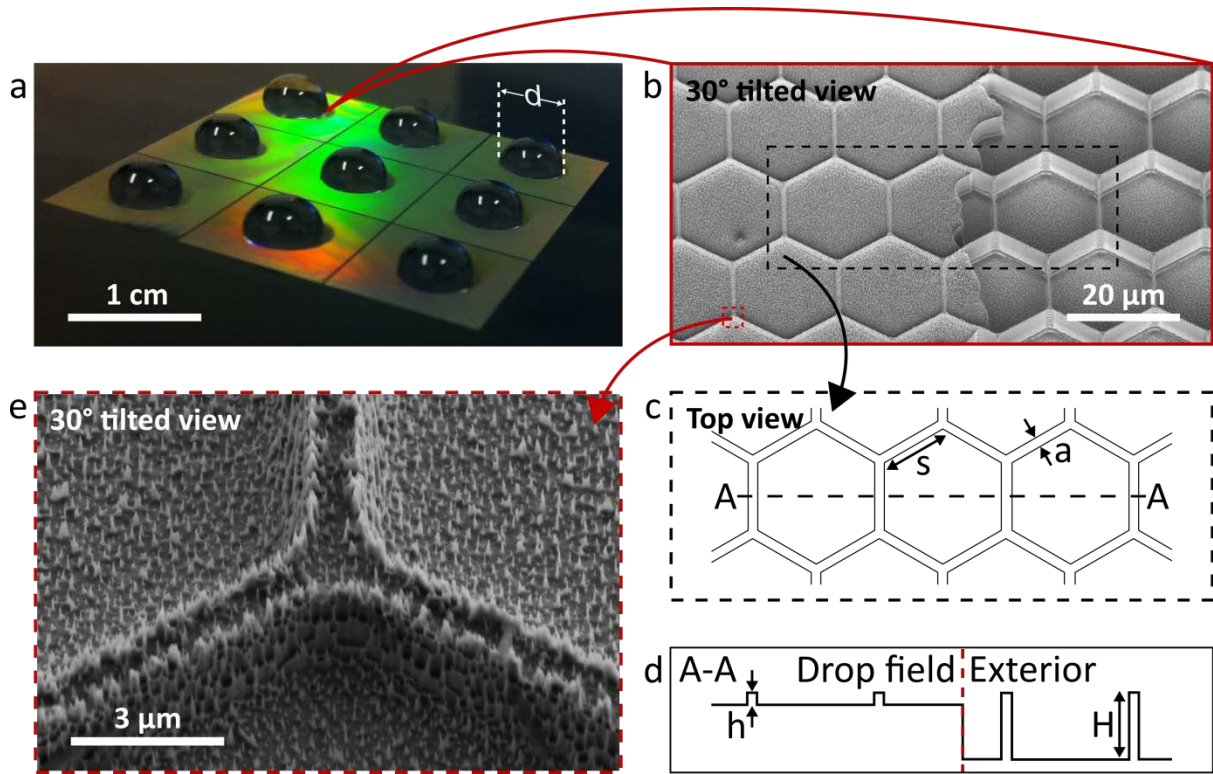


**Figure 1:** An example of an investigated surface and its micro-structures. a) Photograph of a sample surface with self-aligned pipetted drops of base diameter  $d$ . b) 30 degree tilted Scanning Electron Microscopy (SEM) image showing the surface topography including the step in hexagon pit depth from left to right. The drop from (a) is located on the left-hand side, with the lower pits. c) Schematic top view of the used structures with defined hexagon side length  $s$ , and hexagon linewidth,  $a$ . d) Schematic cross-sectional side view of the structures along the A-A line from (c), and with the lower pits having depth  $h$  and the deeper depth  $H$ . E) 30 degree tilted SEM image showing a close-up of (b) for the lower pits.

## Methods

### Fabrication

**Figure 2(a-m)** is a schematic of the fabrication process flow. Surfaces with spatial variance in advancing contact angle were achieved by having hexagonal micro-pits of different depths. The spatial variance in depth was achieved by utilizing a double resist layer. The first layer was a  $\text{SiO}_2$  mask of the hexagonal pattern (a-e). It was fabricated by the following process.[33] (a) Dry oxidation of 100 mm  $\langle 100 \rangle$  n-doped

silicon wafers at 1100°C for 1 hour created an oxide layer of 118 nm. (b) The wafers were then treated with hexamethyldisilazane (HMDS) to enhance adhesion, and subsequently spin coated (Süss MicroTec Gamma 2M spin coater) with 1.5 µm positive tone photoresist (AZ Mir 701). The resist was soft baked at 90 °C for 60 seconds to evaporate residual solvents. Afterward, the resist was exposed for 22 seconds with an intensity of 7.0 mW/cm<sup>2</sup> on a mask aligner (SÜSS MA6) in hard contact mode with the desired hexagonal pattern. (c) The resist was then baked at 110 °C for 60 seconds to maximize process latitudes and to mitigate standing wave effects caused by monochromatic exposure, and hereafter, developed in AZ 726 MIF (Metal Ion Free) for 60 seconds (Süss MicroTec Gamma 2M). (d) The pattern was transferred to the SiO<sub>2</sub> by wet etching in buffered hydrofluoric acid (BHF) for 100 seconds followed by a 5-minute rinse in deionized (DI) water. Lastly, the AZ Mir 701 resist was stripped using plasma ashing (300 Semi Auto Plasma Processor from TePla) with 400 sccm O<sub>2</sub>, 70 sccm N<sub>2</sub>, and 1000 W for 25 minutes. (f-g) The second resist layer was prepared with AZ Mir 701 in the same way as explained for the first. The resist was exposed for 30 seconds in flood exposure mode with a mask placed directly onto the wafers. The mask was made by printing 3 times on top of each other on Premium Transparencies from Xerox with a Xerox 7502V/U printer using the by-pass feeder. The pattern was developed as for the first resist layer. (h) The hexagon pattern in the developed regions was first etched using reactive ion etch (RIE, Pegasus D-RIE, STS, UK) in a Bosch process to a depth of  $H - h$ . (i) The AZ Mir 701 resist was then stripped in the Pegasus in 200 sccm O<sub>2</sub> plasma for 5 minutes. (j) The Bosch process was continued to a depth of  $h$ . (k) The oxide mask was stripped in BHF for 100 seconds with a 5-minute rinse in DI water. (l) In a final RIE process, nanograss was created over the full wafer. The nanograss recipe is obtained from Schneider et al.[25] and uses a mixture of 80 sccm O<sub>2</sub> and 80 sccm SF<sub>6</sub> gas for 8 minutes. (m) Finally, perfluorodecyltrichlorosilane (FTDS) was deposited using molecular vapor deposition (MVD, MVD 100, MST, USA) in order to make the surface hydrophobic.

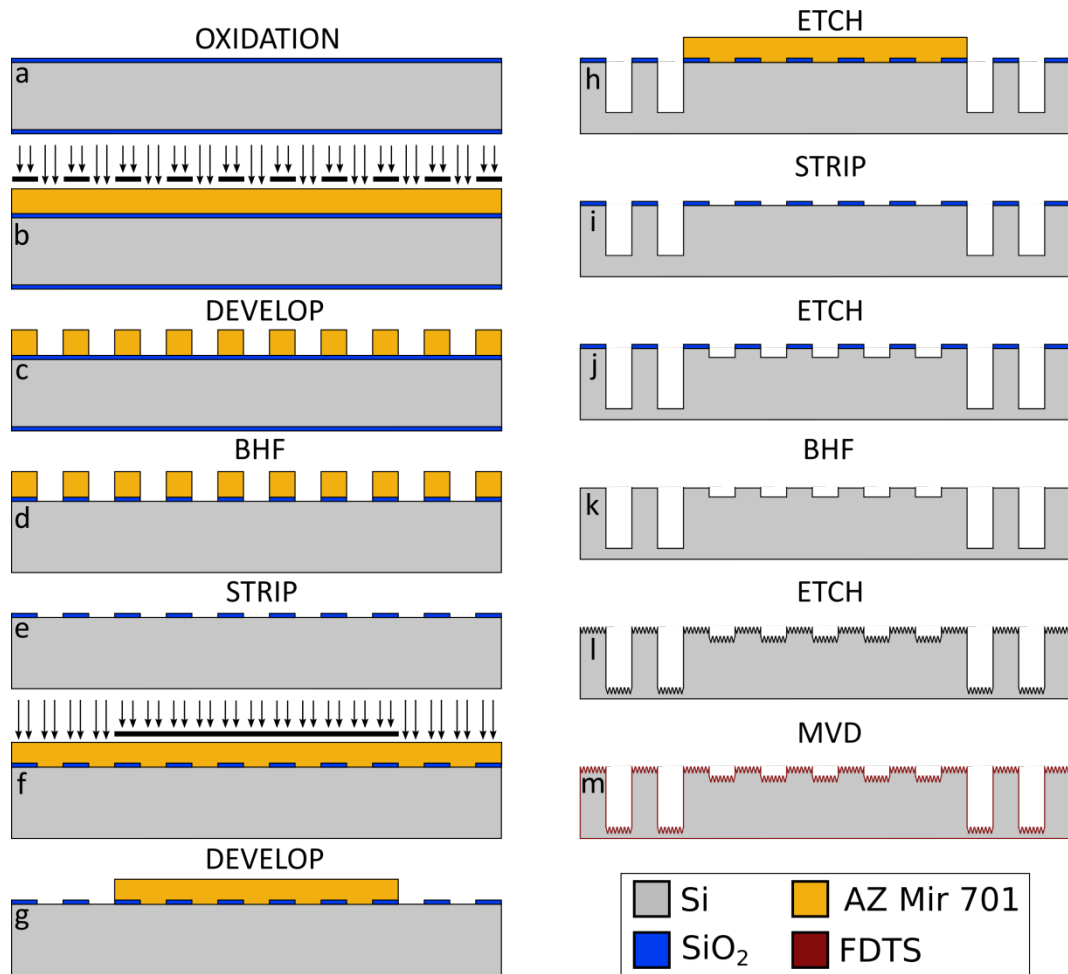


**Figure 2:** Self-explanatory schematic of the sample fabrication yielding the hierarchical surface structure comprising a two-level microstructure fabricated by UV-lithography and deep reactive ion etching (DRIE), superimposed with a random nanograss texture etched into Si, and finally coated with a hydrophobic agent, FDTs.

### Sample characterization

The dimensions of the samples were characterized using SEM. The linewidth,  $a$ , was across all the samples measured to  $(845 \pm 80)$  nm, and the mean hexagon side length,  $s$ , to  $(20.01 \pm 0.08)$   $\mu\text{m}$ . The depths of the micro-pits were calculated by measuring the scallop height for the Bosch process, and multiplying this height with the number of etching cycles. Three samples were prepared with calculated depths,  $h$ , of 0,  $(1.4 \pm 0.1)$ , and  $(5.6 \pm 0.2)$   $\mu\text{m}$ . The deeper pits were all of depth  $H = (7.0 \pm 0.2)$   $\mu\text{m}$ . Before measurements, the substrates were submerged in DI water (Milli-Q) for 1 minute and blow-dried with nitrogen to achieve reproducible results. The data images were collected using an Attension Theta Optical Tensiometer equipped with a high-speed camera (Motion Xtra N3 with Navitar, IDT). DI water drops were pipetted onto the substrates using a motorized dispensing system controlled by Attension Theta software. To document

the self-aligning properties a 100  $\mu\text{L}$  drop was inflated at a rate of 1  $\mu\text{L}/\text{s}$  in a  $d = 5$  mm field. To investigate the effect of the advancing contact angle on the substrate, drops were first inflated at 1  $\mu\text{L}/\text{s}$  from 0 to 30  $\mu\text{L}$  and deflated again at a rate of 0.5  $\mu\text{L}/\text{s}$  (Track B in **Figure 4a**) on a  $d = 3.2$  mm field. Deflation is continued below a critical minimum self-aligned volume where the triple-line starts to contract thus compromising the alignment. Afterward, drops were inflated at 1  $\mu\text{L}/\text{s}$  for 75 seconds to exceed the maximum self-aligned volume (Track A in **Figure 4a**). Video recordings at a rate of 1 frame per second (fps) were performed during both inflation and deflation. The presence of the pipette tip inside the drop is not expected to influence the contact angles significantly.[34] The robustness concerning substrate tilting was investigated using the built-in tilt cradle and tilting at a rate of  $1^\circ/\text{s}$  with 1 fps. From the tilting experiment the pinning force was also estimated. The uncertainty for the slide-off angle,  $\alpha$ , was estimated to be  $1^\circ$ , 1  $\mu\text{L}$  on the volume, and 0.05 mm on the drop field diameter. Using propagation of error for random and independent measurements the uncertainty on the pinning force was then calculated. Between any two measurements the sample was blow-dried with nitrogen for 15 seconds. The substrate had no visual damage after conduction of the experiments, and all measurements were performed 3 times with very high reproducibility. The errorbars in the plots are all determined using the standard sample deviation based on the three measurements series. For all frames the drop base diameter/length was measured using the open source software Tracker 4.9x.

## Results and discussion

We consider the inflation of a microliter-sized drop in a circular micro-nano structured area of diameter  $d$  (see **Figure 1a**). A specific advancing contact angle,  $\theta_{A,in}$ , is present in this inner drop field, and is caused by nanoglass-covered micro-sized hexagon pits of depth  $h$  as seen in (b-e). Exterior to the field the same hexagon geometry is present, but with the pit depth increased to  $H$ . The consequence is an increased advancing contact angle,  $\theta_{A,out}$ .

In the circular region (with  $d = 5$  mm) inflation of a 100  $\mu\text{L}$  drop was performed with an arbitrary pipetting position. Tracking of the distance between the drop center and the field center revealed self-aligning properties. The vanishing misalignment is quantified in **Figure 3**, where the drop has perfect alignment with the field when it has reached a volume of 40  $\mu\text{L}$ . As we shall see later, this self-aligning property is provoked by the step-up in advancing contact angle. The drop is initially (0-21  $\mu\text{L}$ ) expanding in an arbitrary direction dictated by surface defects. When the triple-line of the drop arrives at the transition to the higher advancing contact angle, the barrier against continuous expansion in the given direction increases

significantly, and further expansion must occur in a new direction (21-40  $\mu\text{L}$ ). These changes in growth direction can occur until the triple-line coincide completely with the boundary of the field, and at this point the drop has self-aligned with the field of lower advancing contact angle. The drop stays aligned (within uncertainty) for the remainder of the experiment (40-100  $\mu\text{L}$ ).

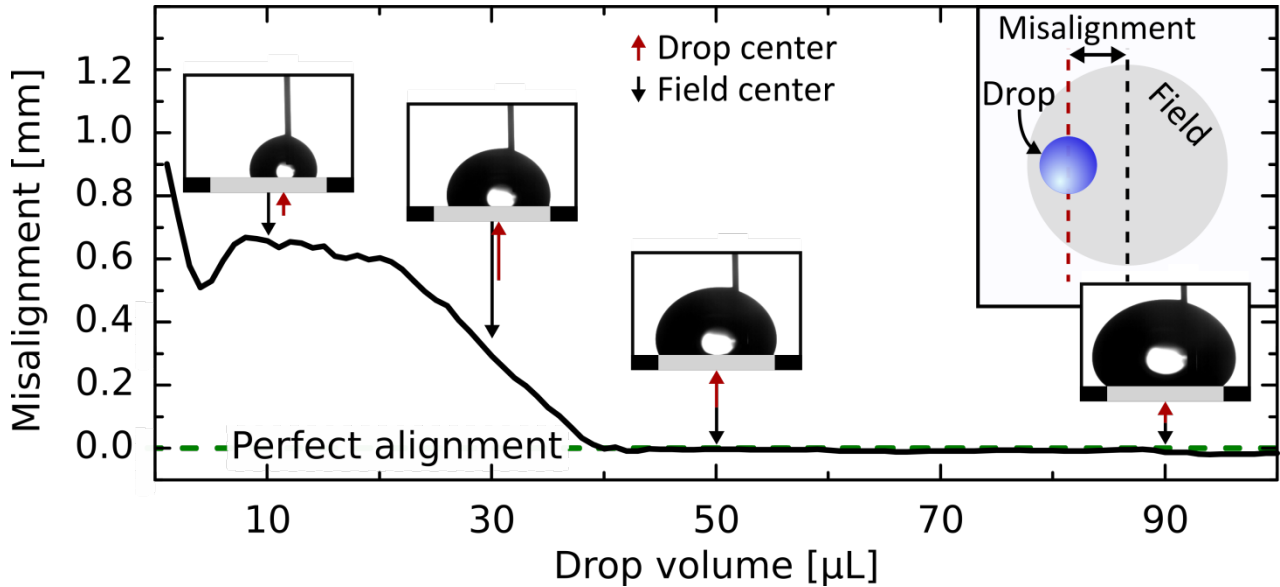


**Figure 3:** Vanishing misalignment of a drop being inflated within the field ( $d = 5 \text{ mm}$ ) of lower advancing contact angle. The upper-right insert shows the field and how the misalignment is defined as the distance between drop center and field center. The 4 drop inserts show the different phases of the drop growth. At 10  $\mu\text{L}$  the growth direction of the drop is governed by structural defects. At 30  $\mu\text{L}$  the drop triple line has been obstructed by the rim of the field, where a step in the advancing contact angle is present. At 50  $\mu\text{L}$  the triple line coincides completely with the field boundary, and the drop has perfect alignment. From 50 to 90  $\mu\text{L}$  the drop stays while the drop volume continuous to grow.

Next, we validate that it is a step in advancing contact angle that causes the self-aligning properties. Surfaces with fixed  $H = 7.0 \text{ }\mu\text{m}$ ,  $s = 20.0 \text{ }\mu\text{m}$ , and  $a = 0.8 \text{ }\mu\text{m}$ , but with different values of  $h$  (0, 1.4, and 5.6  $\mu\text{m}$ ) were fabricated. A drop was inflated from 0 to 75  $\mu\text{L}$  on a  $d = 3.2 \text{ mm}$  field. Both the advancing contact angle and the drop base diameter were measured during the drop inflation. The result can be seen in **Figure 4b**. The two cases with shallower inner hexagon-pits have advancing contact angles,  $\theta_{A,in}$ , significantly different from the advancing contact angle on the outside of the field,  $\theta_{A,out}$  (we define this difference as:  $\Delta\theta_A = \theta_{A,out} - \theta_{A,in}$ ). For  $h = 0$  and 1.4  $\mu\text{m}$   $\Delta\theta_A$  evaluates to  $(47\pm 3)^\circ$  and  $(23\pm 6)^\circ$  respectively. The consequence is an approximately constant contact angle during inflation until the triple line coincides with the field boundary. However, as seen in **Figure 4c**, there seems to be a slight positive correlation between the advancing contact angle and the base diameter during the self-alignment phase,



which has also been observed by Drelich et al. [35, 36] At this point the contact angle increases drastically while the drop base width basically stays constant. The contact angle continues to increase until it matches  $\theta_{A,out}$  and afterward the drop base diameter resumes the increase. This abrupt behavior is completely absent for the  $h = 5.6 \mu\text{m}$  structure, where  $\Delta\theta_A$  is zero within uncertainty. This validates the hypothesis that it is a step in the advancing contact angle that causes the self-aligning properties. We emphasize that it needs to be a step that increases the advancing contact angle in order to make a barrier against further propagation. When a drop was inflated just outside of the field, making  $\Delta\theta_A$  highly negative, we observed on the contrary a pull of the drop far into the field once the triple-line touched the rim of the field.

To take full advantage of this system for self-alignment of pipetted drops, it is crucial to realize the existence of two different tracks of propagation once the drop has self-aligned. This is shown in **Figure 4**. **Figure 4a** illustrates the two tracks of continuation. Track A is a continued inflation. This is also the situation explored in **Figure 4b**. As discussed before, the drop will be aligned with the field until its contact angle matches the advancing contact angle on the exterior,  $\theta_{A,out}$ . At this point the triple-line will initiate movement and its alignment will be lost. Track A gives access to a drop volume as large as possible. However, the triple-line is strongly pinned, which gives the opportunity to deflate the drop rather than continuing the inflation. Track B illustrates this possibility. Also in this case the triple-line will be pinned, and will not contract before the contact angle matches the receding contact angle on the field,  $\theta_{R,in}$ . Utilizing both tracks allows access to a much wider range of drop volumes for a specific design base diameter,  $d$ . The two tracks (A and B) were pursued for  $h = 1.4 \mu\text{m}$ . The result can be seen in **Figure 4c**, and the insert illustrates how the drop inflation is from the region of shallower hexagon pits and towards the deeper ones. Each data point is an average based on 3 measurement series and with associated sample standard deviation plotted as errorbars. It is observed how the drop base diameter keeps expanding until it reaches 3.2 mm. At this point the drop volume continues to change while the drop base diameter is practically fixed. A very low receding contact of the inner field is evident as the drop base diameter does not start to decrease before volumes corresponding to a receding contact angle less than  $10^\circ$ . [37] Thus, as indicated in **Figure 4c**, introducing a step-up in the advancing contact angle, allows a surface with self-aligning properties and with access to any contact angle in a large span; here,  $10^\circ$  to  $164^\circ$ .

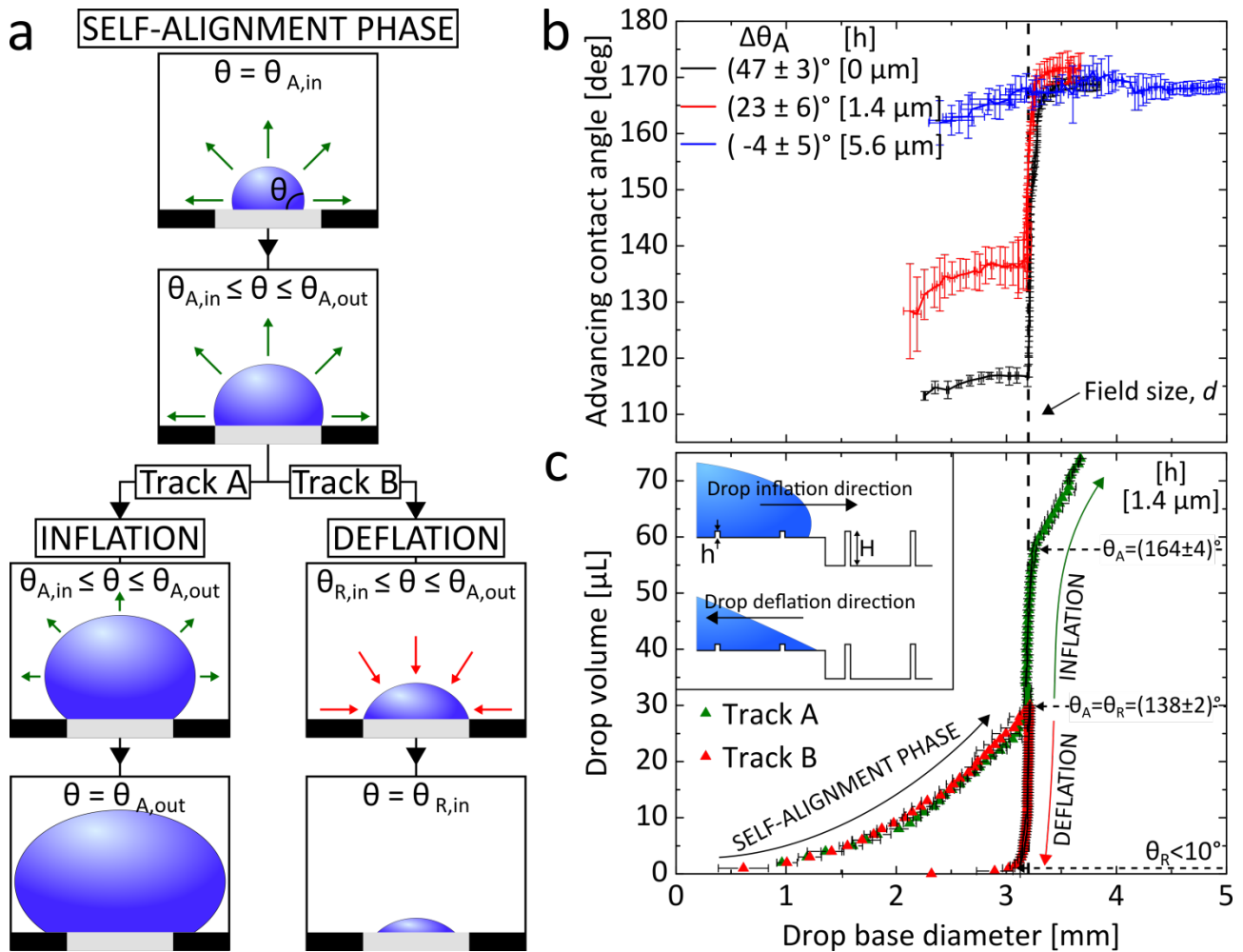


**Figure 4:** a) Schematic showing the initial self-alignment phase and two different tracks A and B to follow once the drop has self-aligned. Track A is a continued inflation and a triple-line being pinned until the critical contact angle,  $\theta_{A,out}$ , is reached. Track B is the choice to deflate the drop while the triple-line stays pinned until the contact angle has decreased to the receding contact angle of the inner field,  $\theta_{R,in}$ . b) Advancing contact angle and drop base diameter measured for a 75  $\mu\text{L}$  drop during inflation on a  $d = 3.2$  mm field. An abrupt change is present for  $h = 0$  and 1.4  $\mu\text{m}$  while absent for  $h = 5.6$   $\mu\text{m}$ .  $\Delta\theta$  is the difference in advancing contact angle on the outer and inner field. c) The pursuit of Track A and B from (a). A 75  $\mu\text{L}$  drop is inflated on the  $h = 1.4$   $\mu\text{m}$  sample for Track A and a 30  $\mu\text{L}$  drop for Track B. The drop base diameter is measured during the inflation and deflation procedure. The insert shows the expansion direction of the inflated drop,

and how it arrives from the shallower pits and approaches the deeper. Also here we clearly see the triple-line stall at a drop base diameter of 3.2 mm.

**Figure 5** addresses the stability of the aligned drop. A tilting experiment was performed, where drops of various sizes were tilted. The drop base length was in each case measured at different tilting angles to find the onset of an irreversible elongation caused by an advancement of the leading drop end. Drops of sizes 30, 35, 40, and 45  $\mu\text{L}$  were tested on  $h = 0 \mu\text{m}$ , and 30 and 40  $\mu\text{L}$  on  $h = 1.4 \mu\text{m}$ . A drop was initially aligned and the substrate was afterward tilted at an angular velocity of 1 degree per second. All drop sizes were tested 3 times. **Figure 5a** shows that the smaller the drop, the larger inclination is needed to cause elongation of the base length. In the investigated domain the onset is believed to be a simple function of the difference between the apparent contact angle,  $\theta$ , for the given drop, and the advancing contact angle on the exterior to the field,  $\theta_{A,out}$ . To validate this hypothesis a linear fit was calculated using between 9 and 15 data points just after the onset of the elongation, and then extrapolation was used to determine the angle equivalent to the initial drop length of 3.2 mm. The initial (for zero tilt) apparent contact angle was also measured, and the error associated was found using the standard sample deviation with the 3 measurements. On the insert in **Figure 5a** the sum of the initial apparent contact angle (CA) and the tilting onset is plotted for the tested volumes. The sum is consistent with the hypothesis of being independent on both structure type and drop volume. A constant fit is made giving a sum value for  $h = 0 \mu\text{m}$  of  $(158 \pm 1)^\circ$ . From **Figure 4b** the exterior advancing contact angle is found to be  $(167 \pm 2)^\circ$ , which is not consistent with the constant fit, suggesting that the model may be qualitatively correct but inadequate. The pinning force for these hierarchical structures are also visualized in **Figure 5b**, where a 50  $\mu\text{L}$  drop on a 5 mm field stays pinned even under vertical tilting conditions. The pinning force (per unit of length) can be calculated from:

$$f = \frac{2V\rho g}{\pi d} \sin \alpha, \quad (1)$$

[38]. Here  $\rho$  is the water density,  $V$  the drop volume,  $\alpha$  the slide-off angle,  $g$  the acceleration of gravity, and  $d$  the field diameter. From the 50  $\mu\text{L}$  vertically pinned drop in **Figure 5b** a lower bound for the pinning force can be found to be  $(63 \pm 3) \text{ mN/m}$ . In **Figure 5a**, we see that drops of 40 and 45  $\mu\text{L}$  in volume for  $h = 0 \mu\text{m}$  slide off the surface at inclination angles  $\alpha$  of  $68^\circ$  and  $59^\circ$  respectively (as determined from the angle where the curves diverge). This allows the pinning force to be estimated by **equation 1** to be  $(72 \pm 2) \text{ mN/m}$  and  $(75 \pm 2) \text{ mN/m}$  respectively. This force is consistent with the previously found lower bound of 63 mN/m from the larger  $d = 5 \text{ mm}$  field, thereby supporting the appropriateness of using a force density to characterize the pinning.

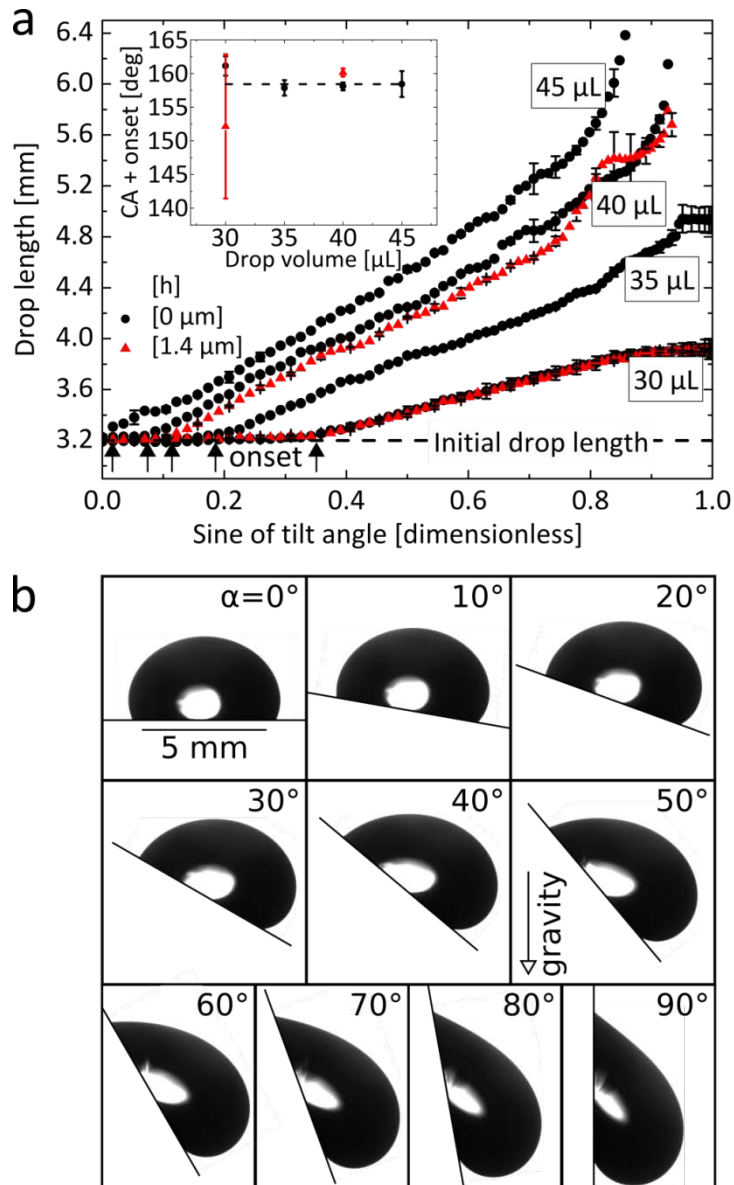


**Figure 5:** a) Drop base length measured for different tilting angles. The drop length is equal to the initial drop length (the length for a zero tilt) until a certain onset (with positions indicated by arrows). The position of the onset clearly depends on the drop volume. The drops measured on are all self-aligned initially causing them to have the same initial base diameter but in return different apparent contact angles. The insert shows the sum of the onset angle and the apparent contact angle for zero tilt. The dashed line is a constant value fit for  $h = 0 \mu\text{m}$  showing how the sum seems independent of both drop volume and structure height,

*h. b) A 50  $\mu\text{L}$  drop on a  $d = 5 \text{ mm}$  region at different tilting angles. The high drop-surface adhesion force causes the drop to stay pinned even under vertical conditions.*

The meaningfulness of using the advancing contact angle for wetting characterization has spawned a long-lasting debate. It has for a long time been the belief that the difference in advancing and receding contact angle, the so-called hysteresis, is a good descriptor for the surface-water adhesive properties. Recent results, however, seem to indicate that for superhydrophobic surfaces only the receding contact angle varies, while the advancing contact angle is invariably  $180^\circ$ . [38, 39] Nevertheless, an interpretation of the apparent contact angle in a drop advancing situation, as being the advancing contact angle still seems to be useful. Our finding, that  $\Delta\theta_A \neq 0$  has a measurable pinning effect for the advancement across the step, shows that the advancing contact angle can differ from  $180^\circ$ , and is not merely a consequence of poor determination of the contact angles. The measuring of a  $<180^\circ$  advancing angle is thus likely a consequence of the drop being in a rose petal type of wetting configuration. This is particularly clear when, as observed, an abrupt change in the conventional advancing contact angle[40] can cause a sudden immobilization of the triple-line. Zhang et al did a numerical study in 2015,[41] where they claimed to have shown that pinning of the triple-line on chemically heterogeneous surfaces is only subject to a slow-down, rather than a complete immobilization. For chemical patterns, this is supported by the Hu et al paper on wettability contrast in 2016.[23] A structural step may however impose a much stronger pinning effect for a drop to pass.

The results presented in this work further provide insight of how to accurately predict the contact angle. Uses of the Wenzel or the Cassie-Baxter equation is far from adequate, as we have observed how the contact angle can be strongly dependent on the drop volume. We have found how the contact angle is a simple function of drop base diameter and drop volume for pinned triple-lines. This independence of the particular surface structures involved is consistent with the work of Liu et al from 2011,[42] who examines exactly this situation and propose a new wetting mechanism when the triple contact line is pinned.

## **Conclusion**

We presented a method to spatially confine a liquid volume and force it to have a specific surface contact area. The confinement was achieved by implementing a step in the advancing contact angle. This acts as an energetic barrier opposing further advancement, which eventually causes the drop triple-line to self-align with the boundary of the designed confinement area. The stability of the self-aligned drop was characterized and we revealed a simple correlation between drop volume and the maximum tilting angle

before compromising the alignment. The water-surface pinning force was measured to be  $(75\pm 2)$  mN/m, which is equivalent to vertical pinning of a  $(38\pm 2)$   $\mu$ L drop on a 3.2 mm circular area. The toolbox to manipulate liquids has been continuously expanded over the past decades. But, only recently have the advancing and receding contact angles received attention. With this work, we contributed in pinpointing the importance of the advancing contact angle properties for pinned rose petal type surfaces.

## References

- [1] Nosonovsky M and Bhushan B 2007 Biomimetic superhydrophobic surfaces: Multiscale approach *Nano Letters* **7** 2633-7
- [2] Mishchenko L, Hatton B, Bahadur V, Taylor J A, Krupenkin T and Aizenberg J 2010 Design of Ice-free Nanostructured Surfaces Based on Repulsion of Impacting Water Droplets *Acs Nano* **4** 7699-707
- [3] Adera S, Raj R, Enright R and Wang E N 2013 Non-wetting droplets on hot superhydrophilic surfaces *Nat Commun* **4**
- [4] Li J, Zhu J and Gao X 2014 Bio-Inspired High-Performance Antireflection and Antifogging Polymer Films *Small* **10** 2578-82
- [5] Yan Y Y, Gao N and Barthlott W 2011 Mimicking natural superhydrophobic surfaces and grasping the wetting process: A review on recent progress in preparing superhydrophobic surfaces *Advances in Colloid and Interface Science* **169** 80-105
- [6] Graham M V and Cady N C 2014 Nano and Microscale Topographies for the Prevention of Bacterial Surface Fouling *Coatings* **4** 37-59
- [7] Di Mundo R, d'Agostino R and Palumbo F 2014 Long-Lasting Antifog Plasma Modification of Transparent Plastics *Acs Applied Materials & Interfaces* **6** 17059-66
- [8] Bhandari P, Narahari T and Dendukuri D 2011 'Fab-Chips': a versatile, fabric-based platform for low-cost, rapid and multiplexed diagnostics *Lab on a Chip* **11** 2493-9
- [9] Dilip D, Jha N K, Govardhan R N and Bobji M S 2014 Controlling air solubility to maintain "Cassie" state for sustained drag reduction *Colloids and Surfaces a-Physicochemical and Engineering Aspects* **459** 217-24
- [10] Cassie A B D and Baxter S 1944 Wettability of porous surfaces *Transactions of the Faraday Society* **40** 0546-50
- [11] Wenzel R N 1936 Resistance of solid surfaces to wetting by water *Industrial and Engineering Chemistry* **28** 988-94
- [12] Barthlott W and Neinhuis C 1997 Purity of the sacred lotus, or escape from contamination in biological surfaces *Planta* **202** 1-8
- [13] Nosonovsky M and Bhushan B 2008 Roughness-induced superhydrophobicity: a way to design non-adhesive surfaces *Journal of Physics-Condensed Matter* **20**
- [14] Bormashenko E, Stein T, Pogreb R and Aurbach D 2009 "Petal Effect" on Surfaces Based on Lycopodium: High-Stick Surfaces Demonstrating High Apparent Contact Angles *Journal of Physical Chemistry C* **113** 5568-72
- [15] Feng L, Zhang Y A, Xi J M, Zhu Y, Wang N, Xia F and Jiang L 2008 Petal effect: A superhydrophobic state with high adhesive force *Langmuir* **24** 4114-9
- [16] Liu K S, Yao X and Jiang L 2010 Recent developments in bio-inspired special wettability *Chemical Society Reviews* **39** 3240-55

- [17] Sogaard E, Andersen N K, Smistrup K, Larsen S T, Sun L and Taboryski R 2014 Study of Transitions between Wetting States on Microcavity Arrays by Optical Transmission Microscopy *Langmuir* **30** 12960-8
- [18] Bhushan B and Nosonovsky M 2010 The rose petal effect and the modes of superhydrophobicity *Philosophical Transactions of the Royal Society a-Mathematical Physical and Engineering Sciences* **368** 4713-28
- [19] Yeh K Y, Cho K H, Yeh Y H, Promraksa A, Huang C H, Hsu C C and Chen L J 2014 Observation of the rose petal effect over single- and dual-scale roughness surfaces *Nanotechnology* **25**
- [20] Ebert D and Bhushan B 2012 Wear-resistant rose petal-effect surfaces with superhydrophobicity and high droplet adhesion using hydrophobic and hydrophilic nanoparticles *Journal of Colloid and Interface Science* **384** 182-8
- [21] Li Q, Zhou P and Yan H J 2016 Pinning-Depinning Mechanism of the Contact Line during Evaporation on Chemically Patterned Surfaces: A Lattice Boltzmann Study *Langmuir* **32** 9389-96
- [22] Kalinin Y V, Berejnov V and Thorne R E 2009 Contact Line Pinning by Microfabricated Patterns: Effects of Microscale Topography *Langmuir* **25** 5391-7
- [23] Hu L, Huang Y, Chen W Y, Fu X and Xie H B 2016 Pinning Effects of Wettability Contrast on Pendant Drops on Chemically Patterned Surfaces *Langmuir* **32** 11780-8
- [24] t Mannelje D, Ghosh S, Lagraauw R, Otten S, Pit A, Berendsen C, Zeegers J, van den Ende D and Mugele F 2014 Trapping of drops by wetting defects *Nature Communications* **5**
- [25] Schneider L, Laustsen M, Mandsberg N and Taboryski R 2016 The Influence of Structure Heights and Opening Angles of Micro- and Nanocones on the Macroscopic Surface Wetting Properties *Scientific Reports* **6**
- [26] Larsen S T, Andersen N K, Sogaard E and Taboryski R 2014 Structure Irregularity Impedes Drop Roll-Off at Superhydrophobic Surfaces *Langmuir* **30** 5041-5
- [27] Sung Y H, Kim Y D, Choi H J, Shin R, Kang S and Lee H 2015 Fabrication of superhydrophobic surfaces with nano-in-micro structures using UV-nanoimprint lithography and thermal shrinkage films *Applied Surface Science* **349** 169-73
- [28] Rytka C, Opara N, Andersen N K, Kristiansen P M and Neyer A 2016 On The Role of Wetting, Structure Width, and Flow Characteristics in Polymer Replication on Micro- and Nanoscale *Macromolecular Materials and Engineering* **301** 597-609
- [29] Telecka A, Murthy S, Schneider L, Pranov H and Taboryski R 2016 Superhydrophobic Properties of Nanotextured Polypropylene Foils Fabricated by Roll-to-Roll Extrusion Coating *ACS Macro Letters* 1034-8
- [30] Murthy S, Matschuk M, Huang Q, Mandsberg N K, Feidenhans'l N A, Johansen P, Christensen L, Pranov H, Kofod G, Pedersen H C, Hassager O and Taboryski R 2016 Fabrication of Nanostructures by Roll-to-Roll Extrusion Coating *Advanced Engineering Materials* **18** 484-9
- [31] Larsen S T and Taboryski R 2009 A Cassie-Like Law Using Triple Phase Boundary Line Fractions for Faceted Droplets on Chemically Heterogeneous Surfaces *Langmuir* **25** 1282-4
- [32] Semprebon C, Varagnolo S, Filippi D, Perlini L, Pierno M, Brinkmann M and Mistura G 2016 Deviation of sliding drops at a chemical step *Soft Matter* **12** 8268-73
- [33] Tanzi S, Ostergaard P F, Matteucci M, Christiansen T L, Cech J, Marie R and Taboryski R 2012 Fabrication of combined-scale nano- and microfluidic polymer systems using a multilevel dry etching, electroplating and molding process *Journal of Micromechanics and Microengineering* **22**
- [34] Seo K, Kim M, Ahn J K and Kim D H 2015 Effects of drop size and measuring condition on static contact angle measurement on a superhydrophobic surface with goniometric technique *Korean Journal of Chemical Engineering* **32** 2394-9
- [35] Drelich J 1997 The effect of drop (bubble) size on contact angle at solid surfaces *Journal of Adhesion* **63** 31-51

- [36] Drelich J, Miller J D and Good R J 1996 The effect of drop (bubble) size on advancing and receding contact angles for heterogeneous and rough solid surfaces as observed with sessile-drop and captive-bubble techniques *Journal of Colloid and Interface Science* **179** 37-50
- [37] Allen J S 2003 An analytical solution for determination of small contact angles from sessile drops of arbitrary size *Journal of Colloid and Interface Science* **261** 481-9
- [38] Paxson A T and Varanasi K K 2013 Self-similarity of contact line depinning from textured surfaces *Nature Communications* **4**
- [39] Schellenberger F, Encinas N, Vollmer D and Butt H J 2016 How Water Advances on Superhydrophobic Surfaces *Physical Review Letters* **116**
- [40] Extrand C W and Kumagai Y 1995 LIQUID-DROPS ON AN INCLINED PLANE - THE RELATION BETWEEN CONTACT ANGLES, DROP SHAPE, AND RETENTIVE FORCE *Journal of Colloid and Interface Science* **170** 515-21
- [41] Zhang J G, Muller-Plathe F and Leroy F 2015 Pinning of the Contact Line during Evaporation on Heterogeneous Surfaces: Slowdown or Temporary Immobilization? Insights from a Nanoscale Study *Langmuir* **31** 7544-52
- [42] Liu J L, Mei Y and Xia R 2011 A New Wetting Mechanism Based upon Triple Contact Line Pinning *Langmuir* **27** 196-200